Digital Current Control in a Rotating Reference Frame—Part I: System Modeling and the Discrete Time-Domain Current Controller With Improved Decoupling Capabilities

Nils Hoffmann, *Member, IEEE*, Friedrich W. Fuchs, *Senior Member, IEEE*, Marian P. Kazmierkowski, *Fellow, IEEE*, and Dierk Schröder, *Fellow, IEEE*

***Abstract*—Digital current control of three-phase voltage-source power electronic converters is analyzed. Special attention is paid to the exact discrete time-domain modeling of inductive-resistive current dynamics in the rotating reference frame whereas three different regular sampling strategies are incorporated to the analysis. The exact system model motivates the development of a new current control structure in the rotating reference frame that is based on discrete time-domain analysis. Ideally, the new discrete time-domain current controller leads to a full compensation of all cross-coupling effects that appear in the controlled system. The experimental results (performed on a 22 kW test-bench) reveal that even under test conditions an excellent decoupling capability of the presented controllers is achieved.**

***Index Terms*—Current control, digital modulation, discrete-time systems, pulse width modulation (PWM) converters, sampling methods.**

I. Introduction

THE key role of three-phase ac-to-dc and dc-to-ac voltage-source power electronic converters in electrical energy and electrical drive systems is indisputable [1]–[4]. Nowadays, power electronic converters are found in a wide range of applications, e.g., in adjustable speed drive systems, renewable energy systems or in electrical energy conditioning systems. Basically, two different areas of frequency operation at the converters ac-side output terminals are identified: 1) constant frequency; and 2) variable frequency operation. Constant frequency operation is usually obtained when power converters are used in grid-tied applications. Variable frequency converter operation is typically attained in motor-tied applications.

Historically, two main schemes have become widely accepted for the control of power converters: in grid-tied applications, the voltage-oriented control (VOC) and in motor-tied applications the field-oriented control (FOC). These control schemes are characterized by cascaded control-loops whereas an inner current control loop is superimposed by outer control loops. For VOC, these outer control-loops are a dc-link voltage control and (if needed) a reactive power control. For FOC, the outer control loops consist of a torque (or speed) controller and (if necessary) a flux controller. Moreover, the existing current control schemes can be classified based on the pulse generation methods applied to create the respective gate drive signals of the semiconductors [5]. In this paper, the current control schemes are divided into two groups: *direct* and *indirect*. The control scheme is classified as direct current control if the current controller manipulates the switching states directly. If a modulator is used to translate the current controller output reference signals into the related semiconductor switching patterns, the control scheme is classified as indirect current control [6].

In steady-state converter operation, a decoupled control of active and reactive current components is achieved by introducing a control scheme in a rotating reference frame. For VOC, this rotating reference frame is aligned to the grid-voltage phase angle and for FOC this reference frame is aligned to the motor-flux (stator-, rotor- or main-flux) rotational angle. However, in transient state converter operation, i.e., in the presence of sudden load variations or high dynamic reference value changes the decoupling capabilities of these aforementioned cascaded control concepts are strongly dependent on the chosen current control concept. For high performance or low pulse-frequency applications, where a high demand of reference value tracking and/or high disturbance value rejection abilities are required the decoupling capabilities of the active and reactive current components become a key parameter driving the overall control design process.

Even though the outer control loops of VOC or FOC utilize the voltage- or flux-orientation principle, the underlying current controllers can be implemented in the stationary ($\alpha\beta$) reference frame, e.g., presented in [7]–[9], or in the rotating (dq) reference frame, e.g., presented in [10]–[14]. However, if the controller

Manuscript received April 19, 2015; revised July 10, 2015; accepted September 1, 2015. Date of publication September 23, 2015; date of current version January 28, 2016. This work was supported in part by the Ministry of Schleswig-Holstein, Germany and in part by the European Union. Further, parts of this work were performed at CEwind e.G. Center of Excellence for wind energy in Schleswig-Holstein. Recommended for publication by Associate Editor F. H. Khan.

N. Hoffmann is with the Department for Research and Product Development, Ingenieurbüro Hoffmann GmbH, Halle/Peißen D-06188, Germany (e-mail: nils.hoffmann@ibrhoffmann.de).

F. W. Fuchs is with the Institute of Power Electronics and Electrical Drives, Christian-Albrechts-University of Kiel, Kiel D-24143, Germany (e-mail: fwf@tf.uni.kiel.de).

M. P. Kazmierkowski is with the Electrotechnical Institute (IEl), Warsaw 04-703 Warsaw, Poland (e-mail: m.kazmierkowski@iel.waw.pl).

D. Schröder is with the Institute for Electrical Drive Systems and Power Electronics, Technische Universität München, Munich D-80333, Germany (e-mail: dierk.schroeder@tum.de).

Color versions of one or more of the figures in this paper are available online at http://ieeexplore.ieee.org.

Digital Object Identifier 10.1109/TPEL.2015.2481726

design and implementation is carried out conscientiously comparable current dynamics are achieved for the current control in stationary or rotating reference frame [15], [16].

This research focuses on the current control in the rotating reference frame whereas special attention is paid to achieve a maximum decoupling capability between be current control of the active- and reactive current components. In the early works [17] and [18], the general problem of applying a standard proportional integral (PI)-based current control into a FOC with variable output frequency operation is addressed. One basic finding of these studies is that the cross-coupling dynamics of current controllers implemented in the rotating reference frame vary with the output frequency at the ac-side terminals of the converter. This aspect is further engrossed in [19] and [20]. Based on a complex vector modeling approach, these two works reveal a deep insight into the origins and effects of cross-coupling dynamics for the current control in the rotating reference frame. Especially, the introduction of the cross-coupling function in [20] provides a straightforward approach to quantify the effects of cross-coupling dynamics.

The relentlessness technological progress of digital signal processors (DSPs) leads to more flexible and more powerful control platforms [7]. These modern control platforms allow high (over-) sampling rates, high computational power, and an enormous amount of variable storage capacity. Therefore, the results in [19]–[21], which are based on continuous time-domain analysis, are transferred to the discrete time domain in [22] giving rise to the discrete nature of modern DSP-based power converter systems. Further, recent publications, e.g. [10] or [23], demonstrate that the current control in the rotating reference frame and the associated cross-coupling dynamics are of high scientific and practical relevance and are not jet fully investigated.

This work aims to contribute to the indirect current control of voltage-source converters in the rotating *dq* reference. More precisely, the novelty of this paper lies in the systematical discrete-time domain analysis of three popular regular sampled pulse width modulation (PWM) schemes as well as of the related dead-time effects and the incorporation of the achieved results in the discrete time-domain current controller synthesis. The special focus of the analysis is set to the discrete time domain and complex vector modeling of inductive-resistive loads which can be operated under constant or variable frequency conditions. Thus, the proposed analysis can be adapted to the control of grid- and motor-connected converter systems.

The overall publication is separated into two parts. Part I (this present work) summarizes the model of the underlying system and the current controller with improved decoupling capabilities that is developed using discrete time-domain and complex vector analysis. Compared to the literature that already presents such analysis, i.e. [22], the proposed approach utilizes a more precise discrete time-domain model of the system under study. This discrete time-domain model also allows incorporating system dead-time effects that are a fraction of the control sampling time. Since this system model is the basis for the proposed current control design, the resultant current controller differs from the works presented in literature so far. In part II of this publication, the proposed discrete time-domain based current controller with improved decoupling capabilities is compared to conventional PI-based current control structures.

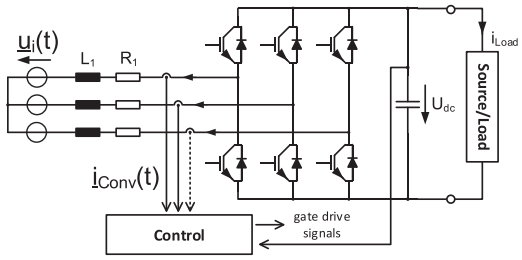

Fig. 1. Schematic block diagram of a voltage-source converter with control of converter ac currents.

This paper is structured as follows: A system description is presented in Section II. The continuous time-domain model of the inductor current dynamics is introduced in Section III. Section IV gives an overview about common regular sampling PWM strategies and Section V discusses the sampling, calculation, and PWM update dynamics based on continuous time-domain modeling. The discrete time-domain model of the aforementioned dynamics considering system dead-time effects that are a fraction for the sampling time is presented in Section VI. The new discrete time-domain current controller with improved decoupling capabilities as well as a experimental validation is shown in Sections VII and VIII. A critical discussion is presented in Section IX. The paper is closed with key conclusions.

II. System Description

Fig. 1 depicts the block diagram of the system under study. A two-level voltage-source converter is considered which is connected to a three-phase three-wire symmetrical voltage system. The converter is composed of six insulated-gate bipolar transistors with the respective gate signals provided by gate drivers and a superimposed control structure. For control feedback purposes and functional safety monitoring, the dc-link voltage U_{DC} and the converter output currents i_{Conv} are measured.

A symmetric three-phase inductive-resistive load with a voltage source is used as an example. The inductive-resistive load can be fed by a constant and/or variable frequency converter operation. For motor-tied applications (commonly variable frequency operation), the power converter acts as a motor drive inverter and for grid-tied applications (regularly constant frequency operation) the power converter operates as an active in-feed converter (AIC).

In motor-tied applications, the load inductance L_1 represents the motors stator leakage inductance and the load resistance R_1 the motors stator winding resistance. Furthermore, the three-phase voltage source u_i is interpreted as the motors counter-electromotive force (or short: back EMF). In general, the motors back EMF depends on the motor type and on the motor's operating point.

In grid-tied applications, the inductive-resistive load model stands for the line-side harmonic-filter. If an *L*-filter is used for grid connection, the load inductance represents the filter

inductance and the load resistance the associated winding resistance. If an *LCL*-filter is applied for grid-connection of the converter, the inductive-resistive load model represents the low frequency model (or the equivalent *L*-filter) of the harmonic filter [24]. Furthermore, the three-phase voltage-source indicates the power networks supply grid voltage.

III. Inductor Current Dynamics

A. Stationary Reference Frame Model

Considering the inductive-resistive load model depicted in Fig. 1 and applying the Clarke-transformation to the illustrated three-phase three-wire system, the following linear differential equation in the stationary $\alpha\beta$ reference frame is derived:

$$\underline{u}_{\mathrm{Conv}}^{\alpha\beta}(t) = R_1 \underline{i}_{\mathrm{Conv}}^{\alpha\beta}(t) + L_1 \frac{d}{dt} \underline{i}_{\mathrm{Conv}}^{\alpha\beta}(t) + \underline{u}_i^{\alpha\beta}(t) \quad (1)$$

where $\underline{u}_{\mathrm{Conv}}^{\alpha\beta}$ describes the complex-valued time-variant vector of the switched converter output voltage in $\alpha\beta$ coordinates, $\underline{u}_i^{\alpha\beta}$ the associated complex-valued time-variant source-voltage vector (motors back EMF or grid supply voltage) in $\alpha\beta$ coordinates, and $\underline{i}_{\mathrm{Conv}}^{\alpha\beta}$ the complex-valued time-variant vector of the converter output current in $\alpha\beta$ coordinates.

The resultant complex-valued transfer function of the converter output voltage to the converter output current (actuating value dynamics) is

$$\underline{G}_{L,F}^{\alpha\beta}(s) = \frac{\underline{I}_{\mathrm{Conv}}^{\alpha\beta}(s)}{\underline{U}_{\mathrm{Conv}}^{\alpha\beta}(s)} = \frac{1}{R_1} \frac{1}{1 + s\frac{L_1}{R_1}} = \frac{1}{R_1} \frac{1}{1 + s\tau_1}. \quad (2)$$

Further, the complex-valued transfer function of the voltage source to the converter output current (disturbance value dynamics) is

$$\underline{G}_{L,S}^{\alpha\beta}(s) = \frac{\underline{I}_{\mathrm{Conv}}^{\alpha\beta}(s)}{\underline{U}_i^{\alpha\beta}(s)} = -\frac{1}{R_1} \frac{1}{1 + s\tau_1}. \quad (3)$$

Both transfer functions describe a first-order time-delay element characteristics.

B. Rotating Reference Frame Model

The focus of this study is set to the indirect current control in the rotating *dq* reference frame. The Park transformation, cf. (4), is applied to transform a generic complex-valued vector $\underline{x}^{\alpha\beta}$ from the stationary $\alpha\beta$ reference frame into the rotating *dq* coordinates $\underline{x}^{dq}$. For variable frequency applications, the angular frequency of the rotating reference frame ω_k is time-variant whereas for constant frequency applications ω_k is time-invariant

$$\underline{x}^{dq}(t) = \underline{x}^{\alpha\beta}(t)\, e^{-j\omega_k t}. \quad (4)$$

If the Park transformation is differentiated, the following transformation results:

$$\frac{d}{dt}\left[\underline{x}^{\alpha\beta}(t)\right] e^{-j\omega_k t} = \frac{d}{dt}\underline{x}^{dq}(t) + j\omega_k \underline{x}^{dq}(t). \quad (5)$$

Using (5), the linear differential equation of the inductive-resistive current dynamics in rotating coordinates may be written as follows:

$$\underline{u}_{\mathrm{Conv}}^{dq}(t) = R_1 \underline{i}_{\mathrm{Conv}}^{dq}(t) + L_1 \frac{d}{dt} \underline{i}_{\mathrm{Conv}}^{\mathrm{dq}}(t) + \underbrace{j\omega_k L_1 \underline{i}_{\mathrm{Conv}}^{dq}(t)}_{\mathrm{cross-coupling}} + \underline{u}_i^{dq}(t). \quad (6)$$

In comparison to the inductive-resistive current dynamics in the stationary reference frame, cf. (1), an additional complex-valued summand appears in the linear differential equation. This term is referred to as a frame speed dependent cross-coupling term [21] since a coupling of the direct transfer dynamics (i.e., *d*- to- *d*-component and *q*- to *q*-component) with the respective orthogonal (indirect) transfer dynamics (i.e. *d*- to *q*-component and *q*- to *d*-components) results

$$\underline{G}_{L,F}^{dq}(s) = \frac{\underline{I}_{\mathrm{Conv}}^{dq}(s)}{\underline{U}_{\mathrm{Conv}}^{dq}(s)} = \frac{1}{R_1} \frac{1}{1 + s\tau_1 + j\omega_k\tau_1}. \quad (7)$$

The complex-valued transfer function of the converter output voltage to the converter output current (actuating value dynamics) in rotating *dq* coordinates is presented in (7). Compared to the transfer characteristics in stationary $\alpha\beta$ coordinates, cf. (2), an additional complex-valued coefficient appears in the transfer functions denominator. This additional coefficient indicates the aforementioned cross-coupling effect.

C. Cross-Coupling Effects

In [20], the cross-coupling function *F* was introduced as one possible figure of merit to qualify and quantify cross-coupling effects. The cross-coupling function is defined as the quotient of the imaginary-part divided by the real-part of a generic complex-valued transfer function. Thus, the cross-coupling function of the considered actuating value dynamics in the rotating *dq* reference frame, cf., (7), is

$$F_{L,F}^{dq}(j\omega) = \frac{\mathrm{Im}\{\underline{G}_{L,F}^{dq}(j\omega)\}}{\mathrm{Re}\{\underline{G}_{L,F}^{dq}(j\omega)\}} = -\frac{\omega_k\tau_1}{1 + j\omega\tau_1}. \quad (8)$$

This cross-function function reveals a low-pass filter dynamics whereas the corner frequency ω_e is calculated to

$$\omega_e = \frac{1}{\tau_1}. \quad (9)$$

The gain magnitude response (in decibel, short: dB) exhibits two characteristic areas. These two characteristic areas are

$$|F_{L,F}^{dq}(j\omega)|_{\mathrm{dB}} = \begin{cases} 20\log(\omega_k\tau_1), & \omega \ll \omega_e \\ 20\log(\omega_k\tau_1) - 20\log(\omega/\omega_e), & \omega \gg \omega_e. \end{cases} \quad (10)$$

Thus, cross-coupling effects emerge for frequencies less than the above presented corner frequency ω_e. Here, the cross-coupling effects become significantly high for systems with a large time constant τ_1 (considering a constant output angular frequency ω_k) or large output angular frequencies ω_k. Typically, applications where these boundary conditions can be observed are (but not limited to these):

1) adjustable-speed drive systems with a regular number of pole-pairs operating at very high rotational speeds;

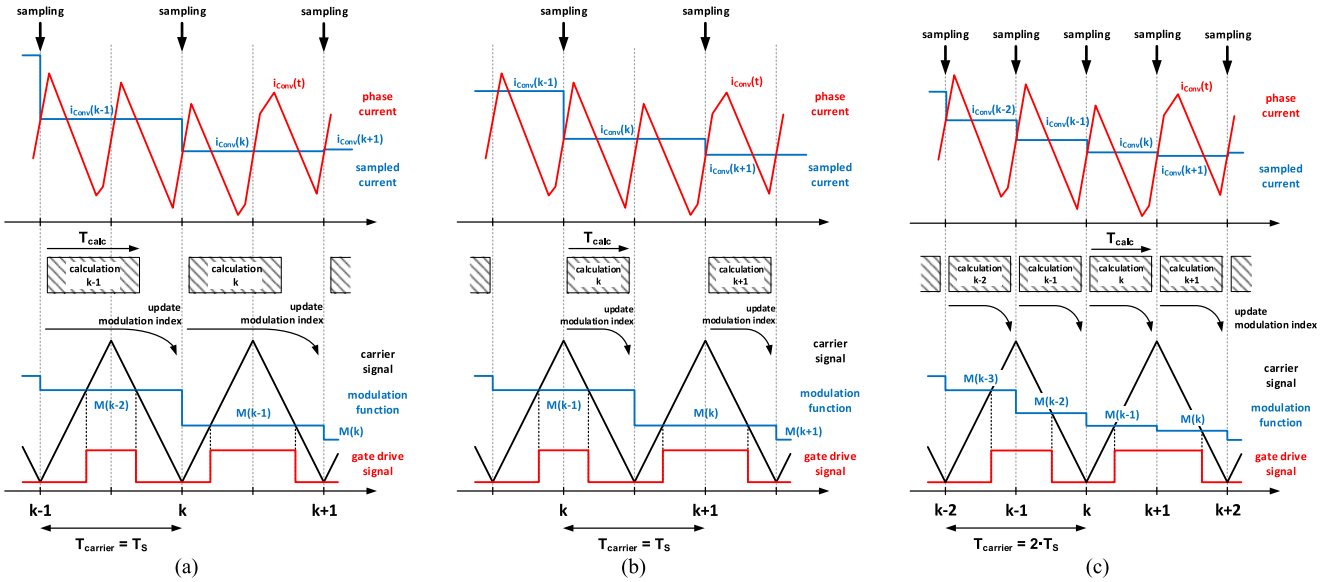

Fig. 2. Schematic one-phase Gantt-diagrams of different regular s-PWM concepts (with identical carrier frequency): (a) symmetrical PWM with sampling at the start of each carrier period (s-PWM-start), (b) symmetrical PWM with sampling in the middle of each carrier period (s-PWM-middle), and (c) asymmetrical PWM with sampling at the start and in the middle of each carrier period (a-PWM-double).

2) adjustable-speed drive systems with a high number of pole-pairs operating at regular rotational speeds;
3) grid-tied or motor-tied converters operating with very low switching frequencies;
4) applications where the motors or filters have a low winding resistance and/or a high inductance.

IV. Regular Sampled PWM Symmetrical PWM Strategies

Indirect current control utilizes additional modulators to translate the reference voltages (output values of the current controller) into the associated semiconductors switching sequences. The choice of a modulator depends on the converter topology, the maximal allowed switching losses, and the harmonic disturbance of the semiconductors switching transitions. For low- to medium-power converter applications PWM is commonly utilized [25] whereas in high-power converter applications with limited switching frequencies pulse-pattern optimized modulation is usually applied [26].

In this paper, indirect current control based on PWM with exemplarily triangular carrier signal is addressed. In general, two fundamental concepts of PWM are found [27]: 1) naturally sampled PWM and 2) regular sampled PWM. These two basic PWM concepts differ in the waveform of the reference voltages. Naturally sampled PWM uses a continuous reference voltage waveform to generate the respective semiconductors switching pattern. Thus, naturally sampled PWM schemes are often found in electronic-based PWM generation circuits. Regular sampled PWM utilizes a sampled reference voltage signal which is the standard practice in software-based PWM generation algorithms.

Regular sampled PWM schemes are further classified based on the symmetry of the generated semiconductors switching signals. If the generated switching patterns are symmetric to the carrier signal, the PWM scheme is referred to as symmetrical regular sampled PWM (s-PWM). If the generated switching signals are asymmetric to the carrier signal, the PWM scheme is referred to as asymmetric regular sampled PWM (a-PWM). Commonly, state of the art DSPs, e.g., the high performance 32-bit Texas Instruments C2000TM DSP series, support three different regular sampled PWM schemes with triangle carrier signals:

1) symmetrical PWM with sampling at the start of each carrier period (s-PWM-start);
2) symmetrical PWM with sampling in the middle of each carrier period (s-PWM-middle);
3) asymmetrical PWM with sampling at the start and in the middle of each carrier period (a-PWM-double).

A. Symmetrical PWM With Sampling at the Start of Each Carrier Period (s-PWM-start)

Fig. 2(a) illustrates the schematic Gantt-diagram of s-PWM-start. More precisely, the timing instants (here: $t = kT_s$) of the phase currents i_{Conv} are illustrated in the top of Fig. 2(a) and the triangle carrier signal, the modulation function and the respective gate drive signals are shown in the bottom of Fig. 2(a). Based on the presented sampling instants (here: two instants are shown) of the phase currents, the required calculation time T_{calc} to process the control algorithms and the resultant modulation index update time instants of the modulation function an overall dead-time T_d between the phase current sampling instant and the PWM update of one sampling period is generated. For s-PWM-start the carrier period T_{carrier} is equal to the sampling period T_s. Thus, the overall dead-time introduced by the sampling, calculation and PWM update routines is

$$T_d|_{\mathrm{s-PWM-start}} = T_{\mathrm{carrier}} = T_s. \tag{11}$$

The sampling instants are synchronized with the triangular carrier signal. More precisely, for s-PWM-start all system states are sampled at the start of the carrier period. Assuming that the zero-state switching vectors are placed symmetrically around the carrier signals minima and maxima the ac current signals are sampled in their mean value. Therefore, the introduced model represents a large-signal model of the inductor current dynamics and the systems sampling and PWM update routines.

B. Symmetrical PWM With Sampling in the Middle of Each Carrier Period (s-PWM-middle)

In Fig. 2(b), the schematic Gantt-diagram of s-PWM-middle is presented. Again, the waveforms of the phase current, the sampled phase current, the triangular carrier signal, the modulation function, and the resultant gate drive signal are denoted for two sampling instants. The sampling instants of all system states are now synchronized in the middle of each carrier signal period. For s-PWM-middle, the time periods of the carrier signal and the systems sampling are equal leading to an overall dead-time T_d introduced by the sampling, calculation, and PWM update routines of

$$T_d|_{\mathrm{s-PWM-middle}} = \frac{1}{2}T_{\mathrm{carrier}} = \frac{1}{2}T_s. \tag{12}$$

Taking the assumption into account that the zero-state switching vectors are placed symmetrically around the carrier signals minima and maxima the ac-current signals are sampled in their mean value resulting again in a large-signal modeling approach of the introduced sampling, calculation and PWM update routine.

C. Asymmetrical PWM With Sampling at the Start and in the Middle of Each Carrier Period (a-PWM-double)

The schematic Gantt-diagram of a-PWM-double is depicted in Fig. 2(c). Now, the principle waveforms of the phase current, the sampled current, the carrier signal, the modulation function, and the gate drive signals are illustrated for four sampling instants. Compared to s-PWM-start and s-PWM-middle, here the modulation function is updated once per carrier signal period, a-PWM-double updates the modulation function twice per carrier signal period. Thus, for a-PWM-double, the carrier signal period time T_{carrier} is doubled in relation to the sampling time period T_s leading to an overall dead-time T_d introduced by the sampling, calculation, and PWM update routines of

$$T_d|_{\mathrm{a-PWM-double}} = \frac{1}{2}T_{\mathrm{carrier}} = T_s. \tag{13}$$

Repeatedly, assuming that the zero state switching vectors are placed symmetrically around the carrier signals minima and maxima the ac-current signals are sampled in their mean value resulting in a large-signal model of a-PWM-double.

D. Asymmetrical PWM With Multiple Sampling and Updating in Every Carrier Period (Multisampled PWM)

Recent works, e.g., those presented in [28] and [29], proposed the concept of multisampled asymmetrical PWM. In contrast to the aforementioned regular sampled PWM strategies, a-PWM with multiple sampling instants ($n > 2$) per carrier signal period does not inherently sample the ac-side phase current in its mean value (even though the zero-state switching vectors are placed symmetrically around the carrier signal extrema). Furthermore, the resultant dead time of multisampled a-PWM depends on the amount of sampling instants per carrier signal period and the specific location of the modulation function in relation to the carrier signal waveforms. Therefore, multisampled a-PWM is not further considered in this paper.

E. Discussion of the Proposed Large-Signal Model

The previous paragraphs introduce the large-signal models of s-PWM-start, s-PWM-middle, and a-PWM-double. Besides the implicit assumption, the PWM methods are operated in the linear or linearized modulation region these large signal models neither consider the specific PWM method (i.e., continuous or discontinuous PWM) nor the PWM's operation point (i.e., the height of the modulation index). These small-signal PWM models are discussed in further studies, e.g., in [7], [28] or [30]–[32], and not presented in this paper.

V. Sampling, Calculation, and PWM Dynamics

A. Stationary Reference Frame Model

The previous analysis reveals that due to the DSPs sampling, calculation and PWM update routines a dead-time T_d is introduced to the control loops. The resultant overall delay time differs based on the applied regular s-PWM strategy. In general, the DSPs sampling, calculation and PWM dynamics in the time domain are described by

$$\underline{u}^{\alpha\beta}_{\mathrm{Conv}}(t) = \underline{u}^{\alpha\beta}_{\mathrm{Conv,ref}}(t - T_d). \tag{14}$$

Here, $\underline{u}^{\alpha\beta}_{\mathrm{Conv}}$ describes the complex-valued time-variant vector of the switched converter output voltage in $\alpha\beta$ coordinates and $\underline{u}^{\alpha\beta}_{\mathrm{Conv,ref}}$ the associated complex-valued time-variant reference voltage vector in $\alpha\beta$ coordinates assigned by the current controller to the PWM. Altogether, the sampling, calculation and PWM update routines lead to a dead-time dynamic. The resultant complex-valued transfer function of the converter reference voltage to the converter output voltage is

$$\underline{G}^{\alpha\beta}_{\mathrm{sample\to update}}(s) = \frac{\underline{U}^{\alpha\beta}_{\mathrm{Conv}}(s)}{\underline{U}^{\alpha\beta}_{\mathrm{Conv,ref}}(s)} = e^{-sT_d}. \tag{15}$$

B. Rotating Reference Frame Model

To achieve a *dq* reference frame formulation of the DSPs sampling, calculation and PWM update dynamics the transformation laws presented in (4) and (5) cannot directly be adapted. More precisely, the dead-time effect has also to be considered for a correct choice of the transformation angle. Since the transformation angle is delayed by the dead-time T_d, the following transformation law between the stationary $\alpha\beta$- and rotating *dq*-coordinates applies

$$\underline{u}^{dq}_{\mathrm{Conv,ref}}(t - T_d) = \underline{u}^{\alpha\beta}_{\mathrm{Conv,ref}}(t - T_d)\, e^{-j\omega_k (t - T_d)}. \tag{16}$$

In consideration of the aforementioned presented transformation law, the complex-valued sampling, calculation and PWM update dynamics in the rotating *dq* reference frame are deduced to

$$\underline{u}^{dq}_{\mathrm{Conv}}(t) = \underline{u}^{dq}_{\mathrm{Conv,ref}}(t - T_d)\, e^{-j\omega_k T_d}. \tag{17}$$

Thus, the resultant complex-valued transfer function in the *dq* coordinates is

$$\underline{G}^{dq}_{\mathrm{sample\to update}}(s) = \frac{\underline{U}^{dq}_{\mathrm{Conv}}(s)}{\underline{U}^{dq}_{\mathrm{Conv,ref}}(s)} = e^{-sT_d}\underbrace{e^{-j\omega_k T_d}}_{\substack{\mathrm{cross}\\ -\mathrm{coupling}}}. \tag{18}$$

Compared to the transfer function in the stationary reference frame, cf., (15), an additional cross-coupling term occurs in the aforementioned presented transfer function.

The fact that the PWM reference voltage is updated only once per sampling period T_s has not been considered so far. This typical sample-and-hold characteristic of all regular sampled PWM schemes is addressed by introducing a zero-order hold-element to the sampling, calculation and PWM update model. A generic zero-order hold frequency domain model is described by

$$\underline{G}^{dq}_{\mathrm{zoh}}(s) = \frac{1 - e^{sT_s}}{s}. \tag{19}$$

The complete frequency domain model of the DSPs sampling, calculation and PWM update routine including the zero-order hold dynamics in rotating *dq* coordinates is now summarized to

$$\begin{aligned}\underline{G}^{dq}_{\mathrm{PWM}}(s) &= \frac{\underline{U}^{dq}_{\mathrm{Conv}}(s)}{\underline{U}^{dq}_{\mathrm{Conv,ref}}(s)} = \underline{G}^{dq}_{\mathrm{zoh}}(s)\,\underline{G}^{dq}_{\mathrm{sample\to update}}(s)\\ &= \frac{1 - e^{sT_s}}{s} e^{-sT_d} e^{-j\omega_k T_d}.\end{aligned} \tag{20}$$

VI. Discrete Time-Domain Modeling

A. Modeling Dead-Time Effects That Are a Fraction of the Sampling Time

Three different regular sampled PWM strategies are discussed in this paper: 1) s-PWM-start; 2) s-PWM-middle; and 3) a-PWM-double. The resultant dead-time T_d introduced by these sampling strategies differs based on the chosen PWM concept. More precisely, for s-PWM-start and a-PWM-double, a dead-time of one sampling period T_s is introduced to the current control loop whereas for s-PWM-middle a dead-time of a half-sampling period is achieved. Thus, for an appropriate mathematical formulation of the discrete time-domain model dead-times that are a fraction (here: $T_d = 1/2T_s$ for s-PWM-middle) of the sampling period have to be considered. To quantify dead-time effects that are a fraction of the sampling period, an auxiliary variable *m* is defined

$$m = 1 - \frac{T_d}{T_s}. \tag{21}$$

Hence:

1) $m = 0$ for s-PWM-start, cf. Fig. 2(a);
2) $m = ½$ for s-PWM-middle, cf. Fig. 2(b);
3) $m = 0$ for a-PWM-double, cf. Fig. 2(c).

In [33], the modeling and effects of a control-delay reduction of digital controlled voltage-source converters are discussed. Here, the use of the modified z-Transformation [34] is suggested to model dead-time effects are a fraction of the sampling time introduced due to a delayed system state sampling strategy. The modified z-Transformation is also adopted in this paper to achieve a generic mathematical formulation of the system under study.

B. Generic Discrete Time-Domain System Model

A complete description of all relevant large signal system dynamics in the continuous time domain is obtained by taking the inductor current dynamics $\underline{G}^{dq}_{L,F}$ (7) as well as the sampling, calculation and PWM-update dead-times $\underline{G}^{dq}_{\mathrm{PWM}}$ (20) into account. Thus, the overall complex-valued transfer function of the system dynamics $\underline{G}^{dq}_{\mathrm{plant}}$ is

$$\begin{aligned}\underline{G}^{dq}_{\mathrm{plant}}(s) &= \frac{\underline{I}^{dq}_{\mathrm{Conv}}(s)}{\underline{U}^{dq}_{\mathrm{Conv,ref}}(s)} = \underline{G}^{dq}_{\mathrm{PWM}}(s)\,\underline{G}^{dq}_{L,F}(s)\\ &= \underbrace{\frac{1 - e^{sT_s}}{s}}_{\substack{\mathrm{digital\ PWM}\\ \mathrm{modulator}}} \underbrace{e^{-sT_d} e^{-j\omega_k T_d}}_{\substack{\mathrm{calculation}\\ \mathrm{dead-time}}} \underbrace{\frac{1}{R_1}\frac{1}{1 + s\tau_1 + j\omega_k\tau_1}}_{\mathrm{inductor\ \ urrent\ dynamics}}.\end{aligned} \tag{22}$$

In general, a discrete time-domain equivalent description of a continuous time-domain based system transfer function is calculated via the transformation law [34]

$$\begin{aligned}\underline{G}^{\,dq}_{\mathrm{plant}}(z,m)\Big|_{m=1-\frac{T_d}{T_s}} &= \frac{\underline{I}^{dq}_{\mathrm{Conv}}(z)}{\underline{U}^{dq}_{\mathrm{Conv,ref}}(z)}\\ &= \mathcal{Z}\left\{\mathcal{L}^{-1}\left\{\underline{G}^{dq}_{\mathrm{plant}}(s)\right\}\Big|_{t=kT_s,}\right\}.\end{aligned} \tag{23}$$

Here, $\mathcal{Z}$ represents the z-Transformation and $\mathcal{L}^{-1}$ the inverse Laplace-Transformation. To apply well-established transformation tables for the z-Transformation, e.g., those presented in [35], further modification of the previously presented transformation law is required. Hence, (23) is manipulated to

$$\begin{aligned}&\underline{G}^{dq}_{\mathrm{plant}}(z,m)\Big|_{m=1-\frac{T_d}{T_s}}\\ &\quad= \frac{z-1}{z}\mathcal{Z}\left\{\mathcal{L}^{-1}\left\{\frac{1}{s}\underline{G}^{\prime dq}_{\mathrm{plant}}(s)\, e^{-sT_d}\right\}\Big|_{t=kT_s}\right\}\\ &\underline{G}^{\prime dq}_{\mathrm{plant}}(s) = \frac{1}{R_1}\frac{1}{1 + s\tau_1 + j\omega_k\tau_1} e^{-j\omega_k T_d}.\end{aligned} \tag{24}$$

For systems where the dead-times T_d are an integer multiplier of the sampling time T_s, the transformation law presented in (24) can directly be applied to calculate the zero-order hold equivalent discrete-time transfer-function $\underline{G}^{dq}_{\mathrm{plant}}(z,m)$. However, as discussed before here dead-times that are a fraction of the systems sampling time appear for s-PWM-middle. Hence, the modified z-Transformation $\mathcal{Z}_{\mathrm{mod}}$ is introduced leading to

TABLE I
COMPLEX-VALUED TRANSFER FUNCTIONS FOR CONTROLLED SYSTEM WITH INDUCTOR CURRENT DYNAMICS AND DIFFERENT SAMPLING STRATEGIES

s-PWM-start [cf. Fig. 2(a), single-update mode, $T_d = T_{\text{carrier}} = T_S$, $m = 0$, $\alpha_2 = 0$]
$\underline{G}^{dq}_{\text{Plant}}(z)\Big\|_{T_d = T_{\text{carrier}} = T_S} = \frac{1}{R_1 + j\omega_k L_1}\frac{1-\alpha_1}{z(z-\alpha_1)} e^{-j\omega_k T_s}$ (25) $\alpha_0 = e^{-T_s/\tau_1} \qquad \alpha_1 = \alpha_0 e^{-j\omega_k T_s}$
s-PWM-middle [cf. Fig. 2(b), single-update mode, $T_d = 1/2T_{\text{carrier}} = 1/2T_S$, m= ½]
$\underline{G}^{dq}_{\text{Plant}}(z)\Big\|_{T_d = \frac{1}{2}T_{\text{carrier}} = \frac{1}{2}T_S} = \frac{1}{R_1 + j\omega_k L_1}\frac{(1-\alpha_2)(z+\alpha_2)}{z(z-\alpha_1)} e^{-j\frac{1}{2}\omega_k T_s}$ (26) $\alpha_0 = e^{-T_s/\tau_1} \qquad \alpha_1 = \alpha_0 e^{-j\omega_k T_s} \qquad \alpha_2 = e^{-\frac{1}{2}T_s/\tau_1} e^{-j\frac{1}{2}\omega_k T_s}$
a-PWM-double [cf. Fig. 2(c), double-update mode, $T_d = 1/2T_{\text{carrier}} = T_S$, $m = 1$]
$\underline{G}^{dq}_{\text{Plant}}(z)\Big\|_{T_d = \frac{1}{2}T_{\text{carrier}} = T_S} = \frac{1}{R_1 + j\omega_k L_1}\frac{1-\alpha_1}{z(z-\alpha_1)} e^{-j\omega_k T_s}$ (27) $\alpha_0 = e^{-T_s/\tau_1} \qquad \alpha_1 = \alpha_0 e^{-j\omega_k T_s}$

the generic transformation laws presented next

$$\underline{G}^{\,dq}_{\,\text{plant}}(z,m)\Big|_{m=1-\frac{T_d}{T_s}} = \frac{z-1}{z}\mathcal{Z}_{\text{mod}}\left\{\mathcal{L}^{-1}\left\{\frac{1}{s}\underline{G}'^{dq}_{\text{plant}}(s)\right\}\Big|_{t=kT_s}\right\}. \quad (28)$$

Based on transformation tables, e.g., those presented in [36], the resultant discrete time-domain complex-valued transfer function of the inductor current dynamics including the dead-time effects introduced by the sampling, calculation and PWM-update dynamics is calculated to

$$\begin{aligned}\underline{G}^{\,dq}_{\,\text{plant}}(z,m)\Big|_{m=1-\frac{T_d}{T_s}} &= \frac{\underline{I}^{dq}_{\text{Conv}}(z)}{\underline{U}^{dq}_{\text{Conv,ref}}(z)} \\ &= \frac{1}{R_1 + j\omega_k L_1}\left[\frac{1}{z} - \frac{\alpha_2(z-1)}{z(z-\alpha_1)}\right] e^{-j\omega_k(1-m)T_s} \\ \alpha_0 &= e^{-T_s/\tau_1} \\ \alpha_1 &= \alpha_0 e^{-j\omega_k T_s} \\ \alpha_2 &= e^{-mT_s/\tau_1} e^{-j\omega_k m T_s}. \end{aligned} \quad (29)$$

In Table I, the resultant complex-valued transfer function for the three previously presented PWM strategies are summarized. Exemplary, the systems transfer function utilizing a-PWM-double, cf. (27), will be briefly analyzed in the following paragraphs. The system gain K_s under steady-state plant conditions is

$$K_s = \underline{G}^{dq}_{\text{plant}}(z=1) = \frac{1}{R_1 + j\omega_k L_1} e^{-j\omega_k T_s}. \quad (30)$$

Considering that the angular frequency of the rotating reference frame ω_k is time variant, the system gain is time variant and complex valued. Moreover, two system poles of the complex-valued transfer function presented in (27) are identified

$$\begin{aligned} z_{\infty,1} &= 0 \\ \underline{z}_{\infty,2} &= \left[\cos(\omega_k T_s) - j\sin(\omega_k T_s)\right] e^{-T_s/\tau_1}. \end{aligned} \quad (31)$$

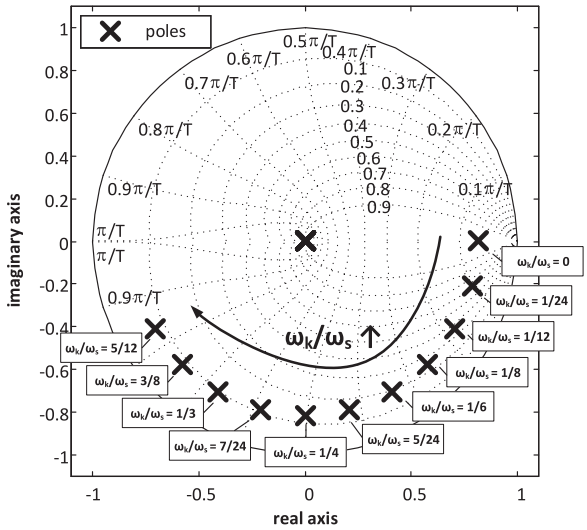

Fig. 3. Complex-valued pole-zero locations of controlled system with current inductor dynamics $\underline{G}^{dq}_{\text{plant}}$ for varying ω_k/ω_S ratios (exemplary chosen: a-PWM-double, $\tau_1 = 8.3$ ms).

Thus, the location of the first system pole $z_{\infty,1}$ is fixed to the origin of the z-domain coordinates whereas the location of the second system pole $\underline{z}_{\infty,2}$ depends on the angular frequency of the rotating reference frame ω_k. Fig. 3 presents the pole-zero locations of the inductive-resistive current dynamics utilizing a-PWM-double (assuming arbitrary system parameters).

Further, to highlight that the location of $\underline{z}_{\infty,2}$ is variable, different ratios between the angular frequency of the rotating reference ω_k and the systems sampling angular frequency $\omega_s(\omega_s = 2\pi/T_s)$ are illustrated.

VII. DISCRETE TIME-DOMAIN CONTROLLER WITH IMPROVED DECOUPLING CAPABILITIES

A. Current Control Concept

The basic structure of the discrete time domain current controller is determined independently from the applied regular sampled PWM concept. Similar to conventional PI-based control approaches, the discrete time-domain current controller should provide a proportional and an integral control path. Further, the underlying structure should enable the possibility to compensate the cross-coupling effects introduced by the aforementioned sampling, calculation and PWM-update routines. Therefore, the structure of the discrete time-domain

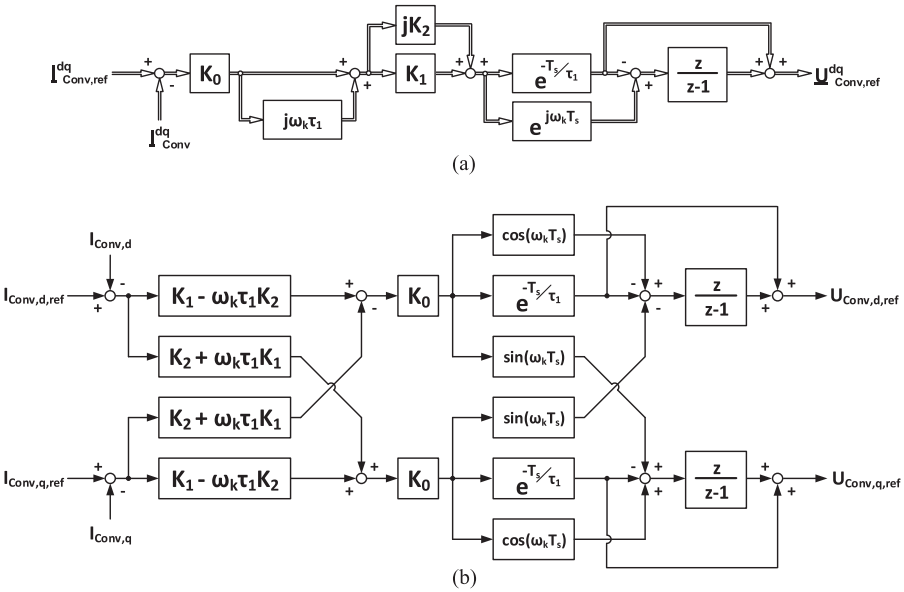

Fig. 4. Block diagram of proposed discrete time-domain current controller with improved decoupling capabilities (valid for s-PWM-start and a-PWM-double): (a) complex and (b) scalar representation.

current controller $\underline{R}(z)$ is set to

$$\begin{aligned}\underline{R}(z) &= \frac{\underline{U}^{dq}_{\mathrm{Conv,ref}}(z)}{\underline{I}^{dq}_{\mathrm{Conv,err}(z)}}\\ &= \underline{K}_{rz}\left[\underbrace{\frac{z}{z-1}}_{\text{integrative}} - \underbrace{\frac{z_0}{z-1}}_{\text{proportional}}\right]\underbrace{e^{j\omega_k T_d}}_{\substack{\text{PWM}\\ \text{decoupling}}}\\ &= \underline{K}_{rz}\frac{z-z_0}{z-1}e^{j\omega_k T_d}. \end{aligned} \tag{32}$$

To attain high command response dynamics and a decoupling of the cross-coupling effects introduced by the inductive-resistive current dynamics, the controllers zero $\underline{z}_0$ is used to compensate the frequency depended system pole $\underline{z}_{\infty,2}$

$$\begin{aligned}\underline{z}_0 &= \alpha_1\\ \alpha_0 &= e^{-T_s/\tau_1}\\ \alpha_1 &= \alpha_0 e^{-j\omega_k T_s}. \end{aligned} \tag{33}$$

Thus, this parameter tuning approach leads to a compensation of the highest systems response time. Furthermore, by allowing the controllers complex-valued zero $\underline{z}_0$ to be adaptive to the angular frequency of the rotating reference frame ω_k, a theoretically ideal decoupling of the inductive-resistive cross-coupling dynamics is achieved.

B. Current Control for s-PWM-start/a-PWM-double

First, the parameter tuning of the discrete time-domain current controller for s-PWM-start and a-PWM-double is presented. Both PWM concepts introduced a dead-time T_d of one sampling period T_s to the control loops. Therefore, the parameter tuning of these two PWM methods is treated equally.

The controllers zero $\underline{z}_0$ is already chosen to compensate the highest system response time and the cross-coupling effects caused by the inductor dynamics. Thus, the complex-valued controller proportional gain $\underline{K}_{rz}$ is used to compensate the system gain $\underline{K}_s$ for steady-state plant conditions. Considering the control plant transfer-functions presented, cf. (25) and (27), as well as the tuning of the controller integral path, cf. (33), the complex-valued proportional gain $\underline{K}_{rz}$ is calculated to

$$\begin{aligned}\underline{K}_{rz} &= K_0\left(1+j\omega_k\tau_1\right)\left(K_1+jK_2\right)\\ K_0 &= \gamma\frac{R_1}{\alpha_0^2 - 2\alpha_0\cos\left(\omega_k T_s\right)+1}\\ K_1 &= 1-\alpha_0\cos\left(\omega_k T_s\right)\\ K_2 &= -\alpha_0\sin\left(\omega_k T_s\right). \end{aligned} \tag{34}$$

Here, an additional real-valued factor $\gamma > 0$ is introduced to shape the command response of the current controller. The block diagram of the proposed discrete time-domain current controller valid for s-PWM-start and a-PWM-double is presented in Fig. 4. In Fig. 4(a), the complex and in (b) the scalar controller representation is shown. Fig. 5 illustrates the calculated step response of the controller for varying values of the tuning factor γ. Further, Table II summarizes the related control characteristics.

Based on the presented structure and the parameter tuning of the discrete time-domain current controller for s-PWM-start and a-PWM-double, the open-loop control transfer function is calculated to

$$\underline{G}^{dq}_{\mathrm{Open-Loop}} = \frac{\gamma}{z^2 - z}. \tag{35}$$

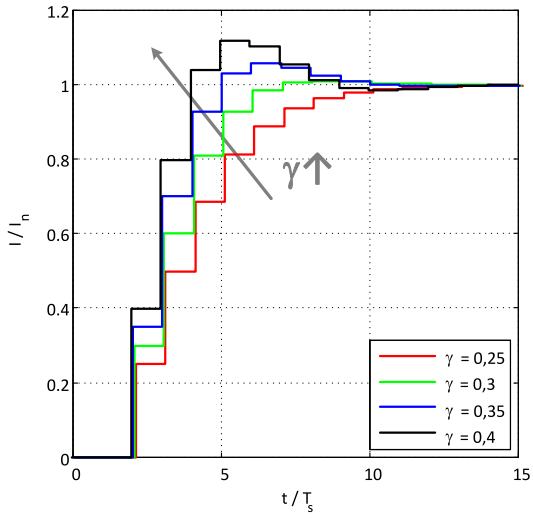

Fig. 5. Calculated step response of the proposed current control for varied values of tuning factor γ (valid for s-PWM-start/a-PWM-double, normalized to sampling time T_s and nominal current I_n).

TABLE II
CONTROL CHARACTERISTICS FOR DIFFERENT VALUES OF TUNING FACTOR AND S-PWM-START/A-PWM-DOUBLE

γ	$\mathrm{bw}_{\mathrm{Hz}}/f_s$	a_{dB} [dB]	φ_R [°]	OS* [%]	T_{rt}^{**}/T_S	T_{st}^{***}/T_S
0.25	0.07	12.0	68	0	6	8
0.30	0.10	10.5	64	1	4	6
0.35	0.13	9.1	60	6	3	7
0.40	0.16	8.0	55	12	2	8

*Overshoot: maximum value during reference step in relation to final steady-state value.
**Rise time: time during reference step to change from 5% to 95% of final steady-state value.
***Settling time: time when controlled value remains within tolerance band of 5% of final state-state value.

Thus, the closed-loop control transfer-function is deduced to

$$\underline{G}^{dq}_{\mathrm{Closed-Loop}} = \frac{\gamma}{z^2 - z + \gamma}. \tag{36}$$

Fig. 6 presents the complex-valued pole-zero locations of the controlled inductor-current dynamics for varied ω_k/ω_s ratios. Both pole-zero maps show the poles and zero of the controlled system in black as well as of the discrete time-domain current controller in red. The pole-zero map of the open-loop control, cf. Fig. 6(a), reveals that the controllers zero location is successfully adapted to the location of the system pole $\underline{z}_{\infty,2}$ which depends on the angular frequency ω_k of the rotating reference frame. The influence of the controller proportional gain $\underline{K}_{rz}$ to the pole-zero location of the closed-loop control is presented in Fig. 6(b). The location of the dominant pole-pair is successfully manipulated by the choice of the real-valued tuning factor γ (here exemplary chosen: $\gamma = 0.35$) without affecting the pole-zero locations of the other system dynamics.

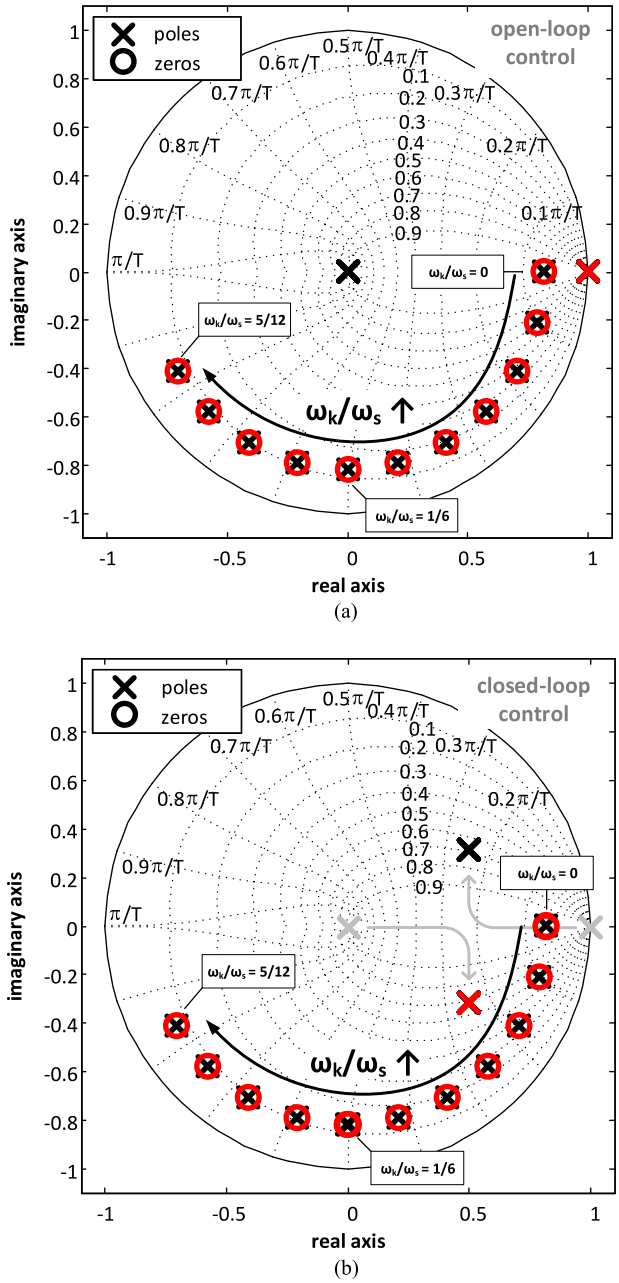

Fig. 6. Complex-valued pole-zero locations of controlled inductor current dynamics for varying ω_k/ω_S ratios (valid for s-PWM-start and a-PWM-double, exemplary chosen: $\gamma = 0.35$, $\tau_1 = 8.3$ ms): (a) open-loop and (b) closed-loop control.

C. Current Control for s-PWM-middle

Second, the parameter tuning of the discrete time-domain current controller for s-PWM-middle is discussed. For s-PWM-middle, an overall dead-time T_d of a half-sampling period T_s is added to the control loops.

Since the controllers integral path is already chosen to compensate the highest system response time, cf. (33), the proportional gain $\underline{K}_{rz}$ is used again to compensate the steady-state system gain. Based on the transfer function of the control plant

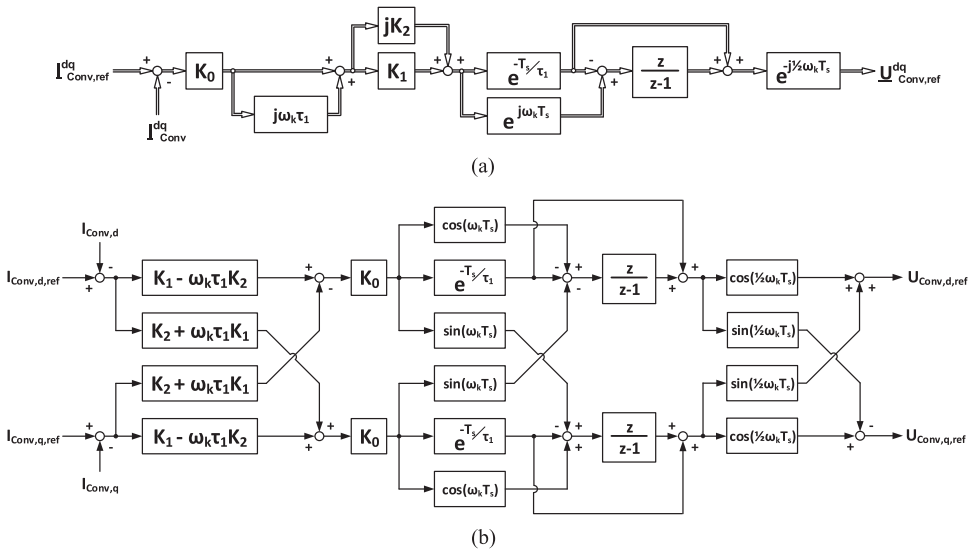

Fig. 7. Block diagram of proposed discrete time-domain current controller with improved decoupling capabilities (valid for s-PWM-middle): (a) complex and (b) scalar representation.

TABLE III
CONTROL CHARACTERISTICS FOR DIFFERENT VALUES OF TUNING FACTOR AND S-PWM-MIDDLE

γ	$\mathrm{bw}_{\mathrm{Hz}}/f_s$	a_{dB} [dB]	φ_R [°]	OS [%]	T_{rt}/T_S	T_{st}/T_S
0.2	0.11	14.0	67	0	4	5
0.25	0.15	12.1	62	4	3	3
0.3	0.19	10.5	58	11	2	6
0.35	0.22	9.2	52	18	2	5

for s-PWM-middle, cf. (26), the complex-valued proportional gain $\underline{K}_{rz}$ is derived to

$$\begin{aligned}\underline{K}_{rz} &= K_0\,(1+j\omega_k\tau_1)\,(K_1+jK_2)\\ K_0 &= \gamma\frac{R_1}{\beta_0^2-2\beta_0\cos\left(\frac{1}{2}\omega_k T_s\right)+1}\\ K_1 &= 1-\beta_0\cos\left(\frac{1}{2}\omega_k T_s\right)\\ K_2 &= -\beta_0\sin\left(\frac{1}{2}\omega_k T_s\right)\\ \beta_0 &= e^{-1/2T_S/\tau_1}.\end{aligned} \tag{37}$$

Again, a real-valued tuning factor $\gamma > 0$ is used to shape the dynamic command response of the proposed current controller. The resultant block diagram including the complex and scalar representation of the discrete time-domain current controller valid for s-PWM-middle is presented in Fig. 7.

Fig. 8 illustrates the analytically calculated step response of the proposed current controller for the system plant utilizing s-PWM-middle for varying tuning factors γ. Furthermore, in Table III, the corresponding control characteristics are summarized.

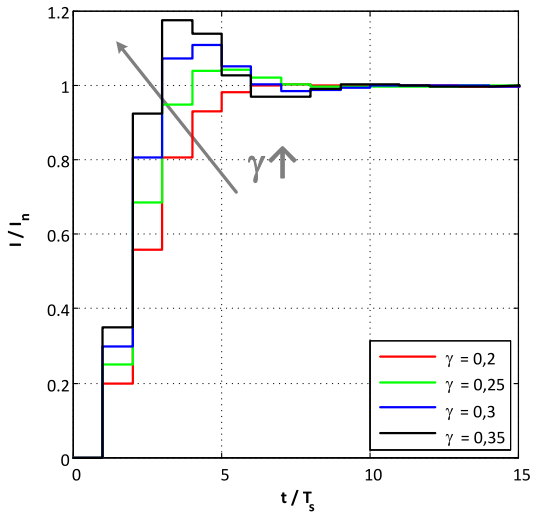

Fig. 8. Calculated step response of the proposed current control for varied values of tuning factor γ (valid for s-PWM-middle, normalized to sampling time T_s and nominal current I_n).

The open-loop control transfer function of the controlled inductor-dynamics for s-PWM-middle is

$$\begin{aligned}\underline{G}^{dq}_{\mathrm{Open-Loop}} &= \frac{\gamma(z+\beta_1)}{z^2-z}\\ \beta_1 &= \beta_0 e^{-1/2\omega_k T_S}.\end{aligned} \tag{38}$$

Further, the closed-loop control transfer function is

$$\underline{G}^{dq}_{\mathrm{Closed-Loop}} = \frac{\gamma\,(z+\beta_1)}{z^2+(\gamma-1)\,z+\beta_1\gamma}. \tag{39}$$

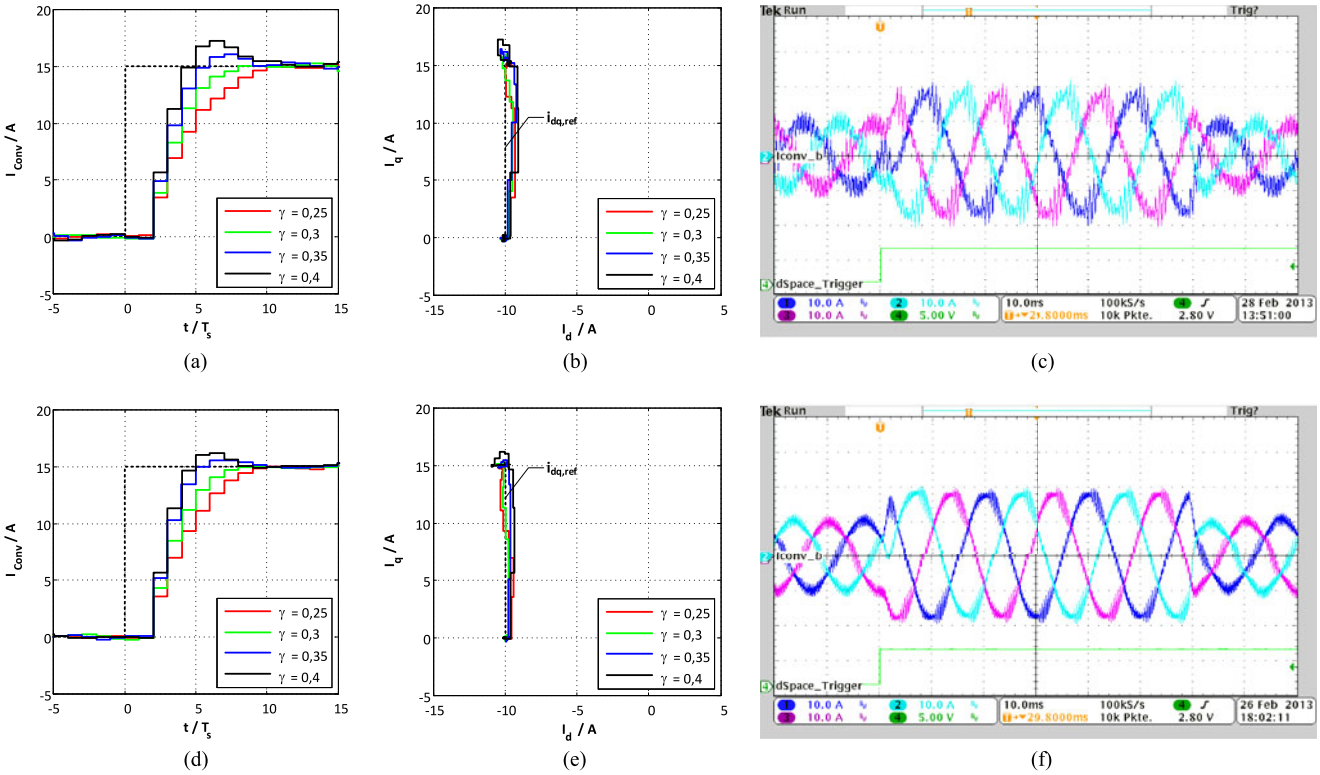

Fig. 9. Measured step response of the proposed discrete current controller with improved decoupling characteristics for different ω_k/ω_S ratios and varied values of tuning factor γ (sampling strategy: s-PWM-start): (a) step response for $\omega_k/\omega_S = 1/27$, (b) step response in *dq*-coordinates for $\omega_k/\omega_S = 1/27$ and $-5 \leq t/T_s \leq 15$, (c) related oscillogram for $\omega_k/\omega_S = 1/27$ and $\gamma = 0.35$, (d) step response for $\omega_k/\omega_S = 1/51$, (e) step response in *dq*-coordinates for $\omega_k/\omega_S = 1/51$ and $-5 \leq t/T_s \leq 15$, and (f) related oscillogram for $\omega_k/\omega_S = 1/51$ and $\gamma = 0.35$.

TABLE IV
MEASUREMENT SYSTEM PARAMETERS

Symbol	Quantity	Value (per unit)
U_{LL}	Line-to-line voltage (rms)	400 V (1.0)
U_{DC}	DC-link voltage	700 V (1.75)
ω_k	Angular line frequency	2π 50 Hz (1.0)
I_n	Rated converter current (rms)	32 A (1.0)
L_1	Line-filter inductance	6 mH (0.35)
R_1	Line-filter resistance	360 mΩ (0.02)
C_{DC}	DC-link capacitance	2200 μF (5.0)

VIII. EXPERIMENTAL RESULTS

A. Test-Bench Description and Test Methodology

A 22-kW test-bench is used to validate the theoretical analysis. The experimental setup consists of a two-level voltage-source converter in back-to-back configuration. The AIC is connected to the laboratory power network using a line-side *L*-filter. To emulate active load conditions, an interior magnet permanent synchronous machine (IPM) which is connected to a four-quadrant converter-fed dc-load machine is used. For all experiments, the IPM is controlled to a constant rotational speed of 1400 r/min. Further, the load torque of the dc machine is adjusted to maintain a constant active power of 5 kW fed into the laboratory grid. In Table IV, a summarization of all relevant system parameters is presented. The control algorithms are implemented on a dSPACE 1006 modular system.

The theoretical analysis reveals that the ω_k/ω_s ratio is crucial in terms of the achievable current control performance. Thus, the measurement analysis is carried out for varied ω_k/ω_s ratios. Further, to simplify the experimental analysis, the current control of the AIC is examined. Therefore, the angular frequency ω_k is dictated by the angular line frequency ω_{line} (here the precondition: $\omega_{\text{line}} = 2\pi 50$ Hz). The choice of the applied ω_k/ω_s ratios for the different PWM schemes is based on the analysis presented in [37] considering the different resultant carrier frequencies f_{carrier} for s-PWM and a-PWM-double. For each *PWM* scheme studied in this paper, two series of measurements are presented using two characteristic ω_k/ω_s ratios. For each series of measurements, reference-value steps of the (reactive) *q*-current component are performed whereas the tuning factor γ is varied.

B. Results

Fig. 9 presents the measured step response of the proposed discrete time-domain current controller for two different ω_k/ω_s ratios whereas the sampling strategy s-PWM-start is applied. In Fig. 9(a)–(c), the experimental results for $\omega_k/\omega_s = 1/27$ (i.e., 50/1350 Hz) and illustrated. Fig. 9(a) presents the measured step response (here: *q*-*q* component) for four characteristic tuning factors γ. The measured step-response validates the

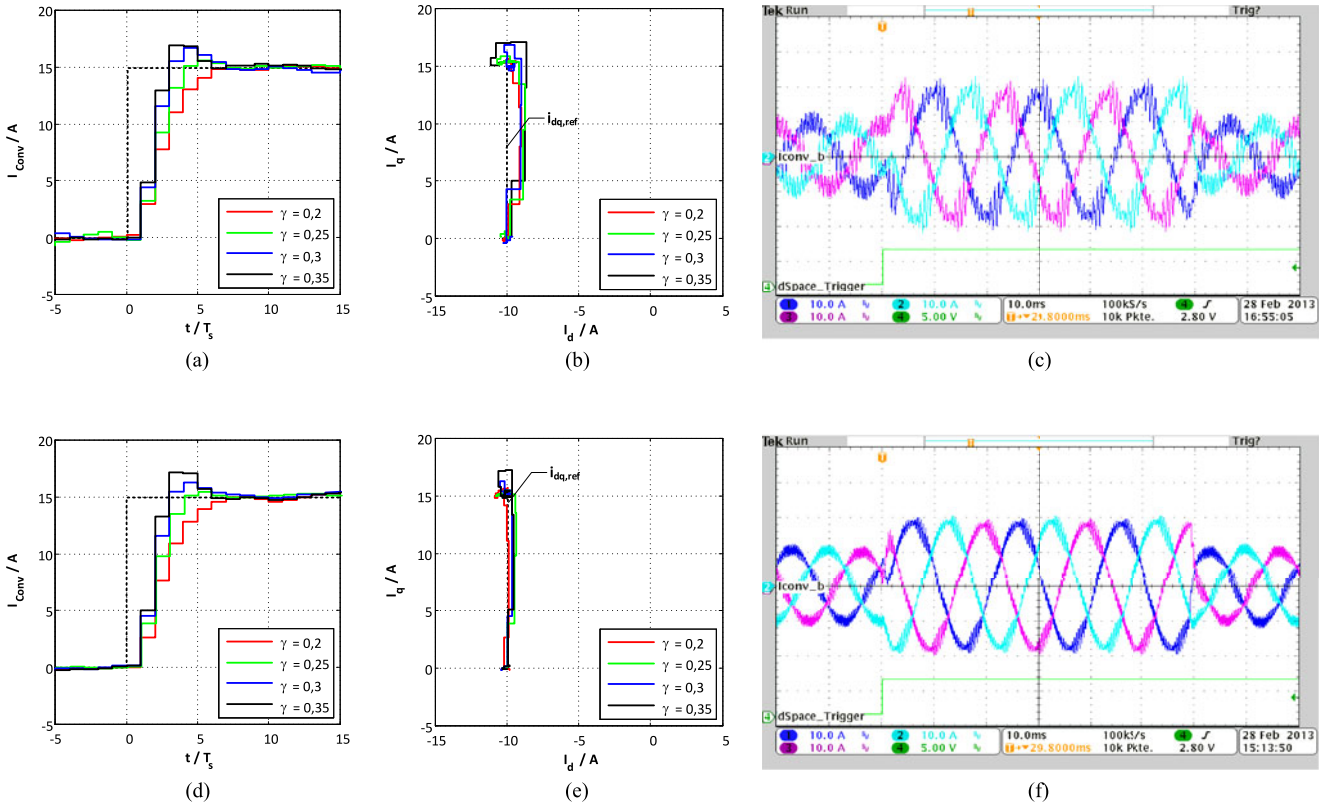

Fig. 10. Measured step response of the proposed discrete current controller with improved decoupling characteristics for different ω_k/ω_S ratios and varied values of tuning factor γ (sampling strategy: s-PWM-middle): (a) step-response for $\omega_k/\omega_S = 1/27$, (b) step-response in *dq*-coordinates for $\omega_k/\omega_S = 1/27$ and $-5 \leq t/T_s \leq 15$, (c) related oscillogram for $\omega_k/\omega_S = 1/27$ and $\gamma = 0.25$, (d) step response for $\omega_k/\omega_S = 1/51$, (e) step response in *dq*-coordinates for $\omega_k/\omega_S = 1/51$ and $-5 \leq t/T_s \leq 15$, and (f) related oscillogram for $\omega_k/\omega_S = 1/51$ and $\gamma = 0.25$.

theoretical analysis. To evaluate the decoupling capabilities of the proposed current control, the measured step-response in *dq*-coordinates is shown in Fig. 9(b). For each considered tuning factor γ, the measured *dq*-current follows the reference-value trajectory revealing only marginal cross-coupling effects. The corresponding oscillogram for $\gamma = 0.35$ and $\omega_k/\omega_s = 1/27$ is presented in Fig. 9(c). Here, the three-phase current waveforms as well as a trigger signal of the preformed reference-step are illustrated.

In Fig. 9(d)–(f), the experimental results for s-PWM-start and $\omega_k/\omega_s = 1/51$ (i.e., 50 Hz/2550 Hz) are summarized. Again, the presented step-responses, cf. Fig. 9(d), and the step-responses in *dq*-coordinates, cf. Fig. 9(e), validate the theoretical analysis. However, an apparently increased decoupling capability for this ω_k/ω_s ratio is observed when the step-responses in *dq*-coordinates are compared to those of $\omega_k/\omega_s = 1/27$. This effect is traced back to two secondary effects which appear when the ω_k/ω_s ratio is varied and the parameters of the line-side *L*-filter are kept constant: 1) The network disturbances introduced by the power converters switching decreases for decreasing ω_k/ω_s ratios due to an increased PWM carrier frequency; and 2) the lower frequency network disturbance rejection capabilities of the current controller increases for decreasing ω_k/ω_s ratios due to an increased sampling frequency. Both effects lead apparently to an increased decoupling capability of the current controller for decreased ω_k/ω_s ratios.

Fig. 10 presents the measurement results for s-PWM-middle considering the same ω_k/ω_s ratios as for s-PWM-start. For both presented series of measurements, the theoretical calculated step-response is validated. Again, an apparently increased decoupling capability for decreased ω_k/ω_s ratios is observed for the measured step-responses *in dq*-coordinates which is traced back to the two aforementioned secondary effects.

The measurement results for a-PWM-double are shown in Fig. 11. For this PWM strategy, the sampling frequency is doubled compared to the carrier-frequency. Considering the analysis presented in [37], here the ω_k/ω_s ratios of 1/30 and 1/54 are chosen to achieve a fair comparison to the former presented measurements results.

Again the measured step responses, cf. Fig. 11(a) and (d), validate the theoretical analysis. Even though that the ω_k/ω_s ratio of 1/30 leads for the system under study to a significantly low effective switching frequency of 750 Hz, an excellent decoupling capability of the proposed current controller is achieved, cf. Fig. 11(b). An apparently increase of the decoupling capabilities for the higher ω_k/ω_s ratio of 1/54, cf. Fig. 11(e), is justified with the decreased network disturbances and the increased disturbance rejection abilities compared to the ω_k/ω_s ratio of 1/30.

To complete the experimental analysis, Fig. 12 presents a comparison between the theoretical calculated and measured step responses for all three examined sampling strategies. More

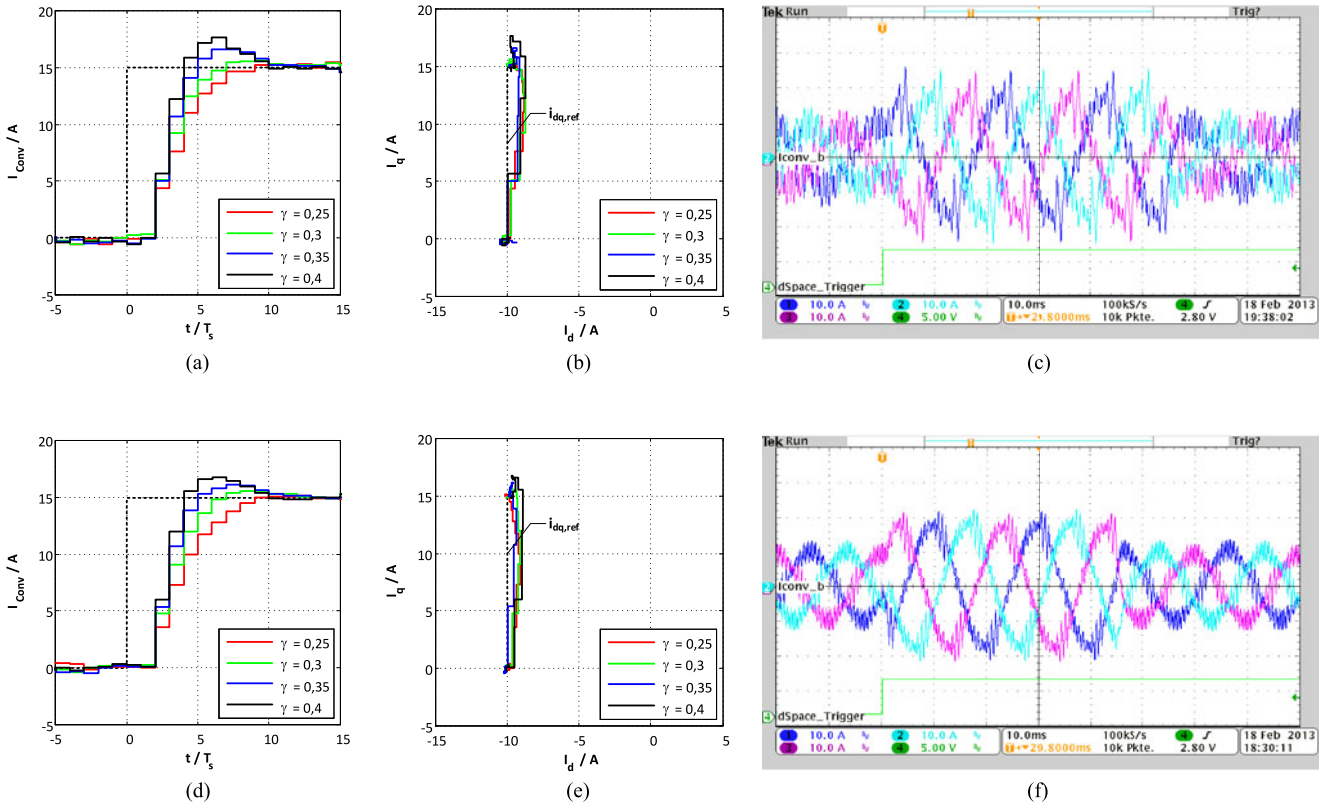

Fig. 11. Measured step response of the proposed discrete current controller with improved decoupling characteristics for different ω_k/ω_S-ratios and varied values of tuning factor γ (sampling strategy: a-PWM-double): (a) step response for $\omega_k/\omega_S = 1/30$, (b) step response in *dq*-coordinates for $\omega_k/\omega_S = 1/30$ and $-5 \leq t/T_s \leq 15$, (c) related oscillogram for $\omega_k/\omega_S = 1/30$ and $\gamma = 0.30$, (d) step response for $\omega_k/\omega_S = 1/54$, (e) step response in *dq*-coordinates for $\omega_k/\omega_S = 1/54$ and $-5 \leq t/T_s \leq 15$, and (f) related oscillogram for $\omega_k/\omega_S = 1/54$ and $\gamma = 0.35$.

precisely, Fig. 12(a) and (b) illustrates the step-responses for s-PWM-start for the two considered ω_k/ω_S ratios (1/27 and 1/51). In Fig. 12(c) and (d), the step response for s-PWM-middle is depicted (ω_k/ω_S ratios 1/27 and 1/51). Further, in Fig. 12(e) and (f), the step-responses for a-PWM-double are presented (ω_k/ω_S ratios 1/30 and 1/54). Altogether, the measured step-responses reveal a very high degree of conformity with the theoretical calculated step-responses almost independent of the applied ω_k/ω_S ratio and the chosen tuning factor γ.

IX. Discussion

The presented analysis in this paper implicitly assumes a symmetrical distribution of the inductive-resistive system parameters for the *d*- and *q*-current control paths. If the system parameters are not distributed symmetrically, e.g., for salient pole synchronous machines, additional transformation networks, e.g., those presented in [38], can be applied to still utilize the proposed current control concept.

Moreover, to improve the disturbance rejection capabilities of the proposed current control concept, an additional disturbance compensation networks, e.g., those presented in [39], can be added to the control loops. This would further counteract the effect of the apparently increased decoupling capability for high ω_k/ω_s ratios.

X. Conclusion

The digital current control of inductive-resistive current dynamics in the rotating reference frame is analyzed. Special attention is paid to the origin and mitigation of cross-coupling effects. Besides the model of the inductive-resistive current dynamics, the analysis incorporates the dynamics of three common regular sampled PWM strategies: 1) s-PWM-start; 2) s-PWM-middle; and 3) a-PWM-double.

A complex-valued vector model of the controlled system is utilized to achieve a clear and compact mathematical formulation that includes all relevant cross-coupling dynamics. The complex-valued system modeling leads to two main cross-coupling effects that appear for the system under study: 1) A cross-coupling effect introduced due to the inductive-resistive current dynamics; and 2) a cross-coupling effect introduced due to the sampling, calculation, and PWM-update routine.

The modified *z*-Transformation is adapted to achieve a model formulation in the discrete time domain. The use of the modified *z*-Transformation is necessary since the sampling strategy s-PWM-middle introduces a dead time to the control loops that is a fraction of the systems sampling time. The resultant discrete time-domain model is formulated for generic fractions of the sampling time. Thus, the presented model is applicable for different control tasks where dead times arise that are a fraction of the sampling time.

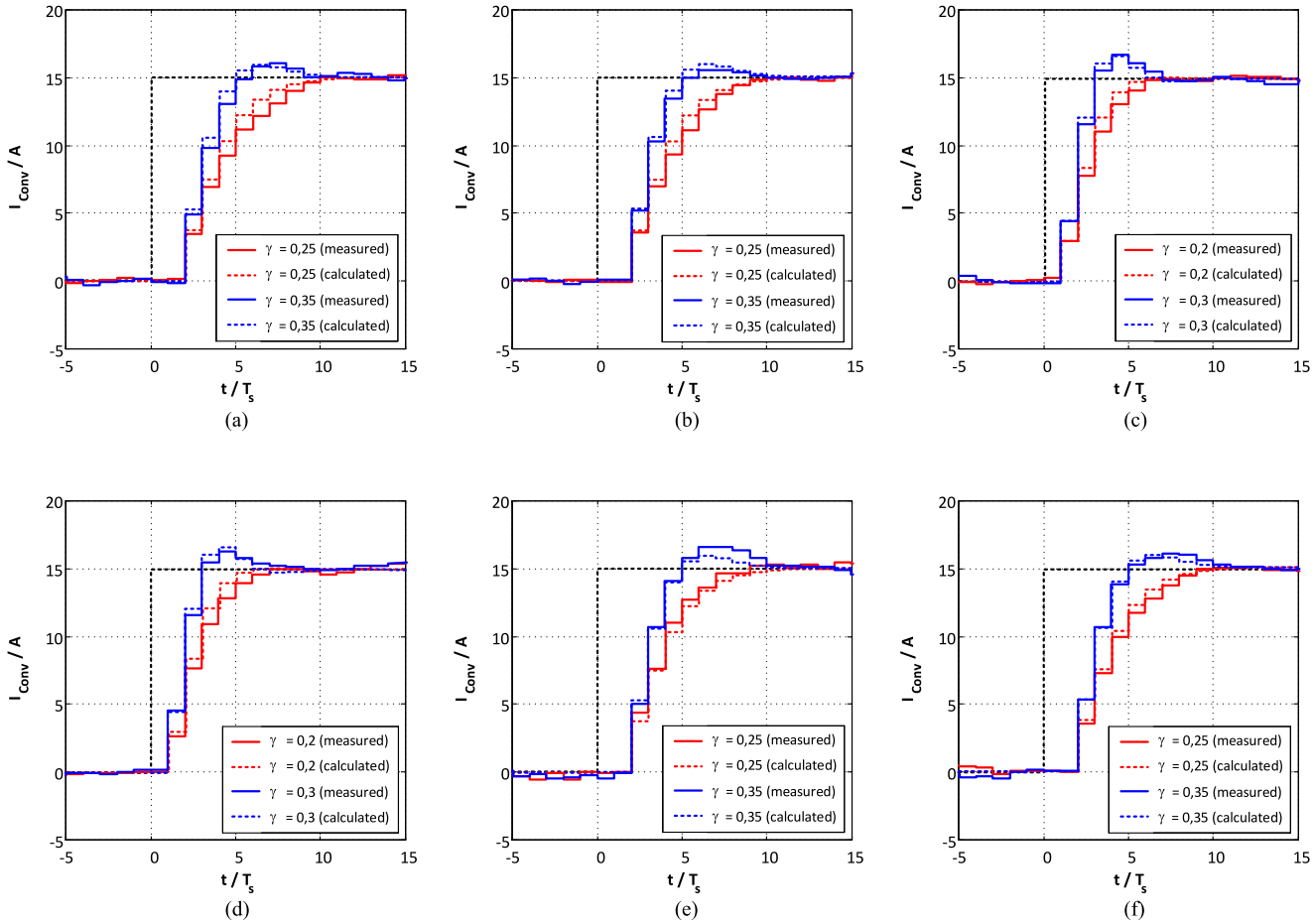

Fig. 12. Comparison between measured and calculated step response of the proposed discrete current controller with improved decoupling characteristics for three different sampling strategies as well as different ω_k/ω_S ratios and varied values of tuning factor γ: (a) s-PWM-start with $\omega_k/\omega_S = 1/27$ and (b) $\omega_k/\omega_S = 1/51$ for $-5 \le t/T_s \le 15$, (c) s-PWM-middle with $\omega_k/\omega_S = 1/27$, and (d) $\omega_k/\omega_S = 1/51$ for $-5 \le t/T_s \le 15$, (e) a-PWM-double with $\omega_k/\omega_S = 1/30$, and (f) $\omega_k/\omega_S = 1/54$ for $-5 \le t/T_s \le 15$.

The exact model of the controlled system motivates the development of a complex-valued current controller that is based on a pure discrete time-domain approach. This new current control strategy is able to compensate the largest systems time constant as well as the related cross-coupling effects for theoretically every ω_k/ω_s ratio. Further, a measurement study performed on a 22 kW test-bench reveals that the proposed discrete time-domain current controller leads to excellent decoupling capabilities.

ACKNOWLEDGMENT

The authors would like to thank Dr. P. B. Thøgersen and Prof. Dr. R. D. Lorenz for their valuable contributions during the theoretical and practical analysis.

REFERENCES

[1] B. K. Bose, "Global energy scenario and impact of power electronics in 21st century," *IEEE Trans. Ind. Electron.*, vol. 60, no. 7, pp. 2638–2651, Jul. 2013.

[2] F. Blaabjerg and K. Ma, "Future on power electronics for wind turbine systems," *IEEE Trans. Emerg. Sel. Topics Power Electron.*, vol. 1, no. 3, pp. 139–152, Sep. 2013.

[3] M. Liserre, T. Sauter, and J. Y. Hung, "Future energy systems: Integrating renewable energy sources into the smart power grid through industrial electronics," *IEEE Ind. Electron. Mag.*, vol. 4, no. 1, pp. 18–37, Mar. 2010.

[4] P. K. Steimer, "Power electronics, a key technology for future more electrical energy systems," in *Proc. IEEE Energy Convers. Cong. Expo.*, 2009, pp. 1161–1165.

[5] M. P. Kazmierkowski and L. Malesani, "Current control techniques for three-phase voltage-source PWM converters: A survey," *IEEE Trans. Ind. Electron.*, vol. 45, no. 5, pp. 691–703, Oct. 1998.

[6] D. Schröder, *Elektrische Antriebe—Regelung von Antriebssystemen*, 4th ed. Berlin, Germany: Springer-Verlag, 2015, (in German).

[7] S. Buso and P. Mattavelli, *Digital Control Power Electronics*, San Mateo, CA, USA: Morgan & Claypool Publishers, 2006.

[8] D. G. Holmes, T. A. Lipo, B. P. McGrath, and W. Y. Kong, "Optimized design of stationary frame three phase AC current regulators," *IEEE Trans. Power Electron.*, vol. 24, no. 11, pp. 2417–2426, Nov. 2009.

[9] A. Lopez De Heredia, H. Gaztanaga, I. Etxeberria-Otadui, S. Bacha, and X. Guillaud, "Analysis of multi-resonant current control structures and tuning methods," in *Proc. 32nd Annu. Conf. IEEE Ind. Electron.*, 2006, pp. 2156–2161.

[10] B. Bahrani, S. Kenzelmann, and A. Rufer, "Multivariable-PI-Based dq current control of voltage source converters with superior axis decoupling capability," *IEEE Trans. Ind. Electron.*, vol. 58, no. 7, pp. 3016–3026, Jul. 2011.

[11] B. Bahrani,, A. Karimi, B. Rey, and A. Rufer, "Decoupled dq-current control of grid-tied voltage source converters using nonparametric models," *IEEE Trans. Ind. Electron.*, vol. 60, no. 4, pp. 1356–1366, Apr. 2013.

[12] J. Böcker, S. Beineke, and A. Bahr, "On the control bandwidth of servo drives," in *Proc. 13th Eur. Conf. Power Electron. Appl.*, 2009, pp. 1–10.

[13] N. Hoffmann, F. W. Fuchs, and J. Dannehl, "Models and effects of different updating and sampling concepts to the control of grid-connected PWM converters—A study based on discrete time domain analysis," in *Proc. 14th Eur. Conf. Power Electron. Appl.*, 2011, pp. 1–10.
[14] A.G. Yepes, A. Vidal, J. Malvar, O. Lopez, and J. Doval-Gandoy, "Tuning method aimed at optimized settling time and overshoot for synchronous proportional-integral current control in electric machines," *IEEE Trans. Power Electron.*, vol. 29, no. 6, pp. 3041–3054, Jun. 2014.
[15] D. G. Holmes, B. P. McGrath, and S. G. Parker, "A comparative evaluation of high performance current regulation strategies for vector controlled induction motor drives," in *Proc. IEEE Int. Symp. Ind. Electron.*, 2010, pp. 3707–3714.
[16] C. H. Van Der Broeck, R. W. De Doncker, S. A. Richter, and J. von Bloh, "Discrete time modeling, implementation and design of current controllers," in *Proc. IEEE Energy Convers. Cong. Expo.*, 2014, pp. 540–547.
[17] D.-C. Lee, S.-K. Sul, and M.-H. Park, "High performance current regulator for a field-oriented controlled induction motor drive," *IEEE Trans. Ind. Appl.*, vol. 30, no. 5, pp. 1247–1257, Sep. 1994.
[18] J. Böcker, J. Janning, and K. Anbuhl, "Realization of a high-dynamic discrete-time controller for PWM inverter-fed induction motor drives," in *Proc. 5th Eur. Conf. Power Electron. Appl.*, 1993, pp. 158–162.
[19] F. Briz, M. W. Degner, and R. D. Lorenz, "Analysis and design of current regulators using complex vectors," *IEEE Trans. Ind. Appl.*, vol. 36, no. 3, pp. 817–825, May 2000.
[20] J. Holtz, J. Quan, J. Pontt, J. Rodriguez, P. Newman, and H. Miranda, "Design of fast and robust current regulators for high-power drives based on complex state variables," *IEEE Trans. Ind. Appl.*, vol. 40, no. 5, pp. 1388–1397, Sep. 2004.
[21] F. Briz, M. W. Degner, and R. D. Lorenz, "Dynamic analysis of current regulators for AC motors using complex vectors," *IEEE Trans. Ind. Appl.*, vol. 35, no. 6, pp. 1424–1432, Nov./Dec. 1999.
[22] H. Kim, M. W. Degner, J. M. Guerrero, F. Briz, and R. D. Lorenz, "Discrete-time current regulator design for AC machine drives," *IEEE Trans. Ind. Appl.*, vol. 46, no. 4, pp. 1425–1435, Jul. 2010.
[23] A. G. Yepes, A. Vidal, O. Lopez, and J. Doval-Gandoy, "Evaluation of techniques for cross-coupling decoupling between orthogonal axes in double synchronous reference frame current control," *IEEE Trans. Ind. Electron.*, vol. 61, no. 7, pp. 3527–3531, Jul. 2014.
[24] M. Liserre, A. Dell'Aquila, and F. Blaabjerg, "Stability improvements of an LCL-filter based three-phase active rectifier," in *Proc. IEEE Power Electron. Spec. Conf.*, 2002, vol. 3, pp. 1195–1201.
[25] J. Holtz, "Pulsewidth modulation for electronic power conversion," *Proc. IEEE*, vol. 82, no. 8, pp. 1194–1214, Aug. 1994.
[26] G. S. Buja and G. B. Indri, "Optimal pulsewidth modulation for feeding AC motors," *IEEE Trans. Ind. Appl.*, vol. IA-13, no. 1, pp. 38–44, Jan. 1977.
[27] D. G. Holmes and T. A. Lipo, *Pulse Width Modulation Power Converters: Principles Practice*. Hoboken, NJ, USA: Wiley, 2003.
[28] L. Corradini, E. Tedeschi, and P. Mattavelli, "Advantages of the symmetric-on time modulator in multiple-sampled digitally controlled DC-DC converters," in *Proc. IEEE Power Electron. Spec. Conf.*, 2007, pp. 1974–1980.
[29] L. Corradini, W. Stefanutti, and P. Mattavelli, "Analysis of multisampled current control for active filters," *IEEE Trans. Ind. Appl.*, vol. 44, no. 6, pp. 1785–1794, Nov. 2008.
[30] S. Hiti and D. Boroyevich, "Small-signal modeling of three-phase PWM modulators," in *Proc. IEEE Power Electron. Spec. Conf.*, 1996, pp. 550–555.
[31] P. W. Lehn, "Exact modeling of the voltage source converter," *IEEE Trans. Power Del.*, vol. 17, no. 1, pp. 217–222, Jan. 2002.
[32] D. M. Van De Sype, K. De Gusseme, F. M. L. L. De Belie, A. P. van den Bossche, and J. A. Melkebeek, "Small-signal z-domain analysis of digitally controlled converters," *IEEE Trans. Power Electron.*, vol. 21, no. 2, pp. 470–478, Mar. 2006.
[33] P. Mattavelli, F. Polo, F. Dal Lago, and S. Saggini, "Analysis of control-delay reduction for the improvement of UPS voltage-loop bandwidth," *IEEE Trans. Ind. Electron.*, vol. 55, no. 8, pp. 2903–2911, Aug. 2008.
[34] E. I. Jury, *Theory Application z-Transform Method*. Hoboken, NJ, USA: Wiley, 1964.
[35] H. Lutz and W. Wendt, *Taschenbuch der Regelungstechnik*, 7th ed. Berlin, Germany: Verlag Harri Deutsch, 2007.
[36] B. K. Kuo, *Digital Control Systems (The Oxford Series in Electrical and Computer Engineering)*, 2nd ed., London, U.K.: Oxford Univ. Press, 1995.
[37] F. Wang, "Reduce beat and harmonics in grid-connected three-level voltage-source converters with low switching frequencies," *IEEE Trans. Ind. Appl.*, vol. 43, no. 5, pp. 1349–1359, Sep. 2007.
[38] Y.-S. Jeong and S.-K. Sul, "Analysis and design of a decoupling current controller for AC machines: A unified transfer-matrix approach," in *Proc. 14th IAS Annu. Meet. Ind. Appl. Conf.*, 2005, pp. 751–758.
[39] K. Lee, T. M. Jahns, T. A. Lipo, V. Blasko, and R. D. Lorenz, "Observer-based control methods for combined source-voltage harmonics and unbalance disturbances in PWM voltage-source converters," *IEEE Trans. Ind. Appl.*, vol. 45, no. 6, pp. 2010–2021, Nov. 2009.

Nils Hoffmann (S'09–M'14) was born in Halle/Saale, Germany, in 1983. He received the Dipl.-Ing. and Dr.-Ing. degrees from the Christian-Albrechts-University of Kiel, Kiel, Germany, in 2009 and 2014, respectively.

Between 2009 and 2013, he was with the Institute of Power Electronics and Electrical Drives, Christian-Albrechts-University of Kiel, working on modern control strategies applied to grid-connected power converter systems. Since 2013, he has been with the Ingenieurbüro Hoffmann GmbH in Halle/Saale, where he is the Head of research and product development for power electronics and electrical drives. His work involves modern and innovative concepts of power electronic systems, electrical drives and renewable energy applications with the focus on technological consulting, assistance in problem cases, feasibility studies, preliminary and ready-to-release system designs, prototyping as well as fundamental and advanced training services. His main research interests include the control of power converters and drives, power quality in distributed power generation networks and modern multilevel converter topologies for high power adjustable speed drive applications.

Dr. Hoffmann is one recipient of the 2014 best paper award of the German VDE Power Engineering Society. Further, his Ph.D. thesis entitled "Grid-adaptive control and active-filter functionality of grid-connected PWM converters in renewable energy generation" was honored with the grade "summa cum laude" in 2014. He is an active Member of the IEEE Power Electronics Society, the IEEE Industrial Electronics Society, the IEEE Industry Applications Society as well as of the VDE Power Engineering Society.

Friedrich W. Fuchs (M'96–SM'01) received the Dipl.Ing. and Ph.D. degrees from the Rheinisch-Westfaelische Technische Hochschule (University of Technology), Aachen, Germany, in 1975 and 1982, respectively.

Between 1975 and 1982, he was with the University of Aachen, Aachen, where he was involved in research on ac automotive drives. From 1982 to 1991, he was a Group/Department Manager involved in research on the development of power electronics and electrical drives in a medium-sized company. In 1991, he became the Managing Director of the Converter and Drives Division (presently, GE Power Conversion), Allgemeine Elektrizitaets-Gesellschaft, Berlin, Germany, in the area of design and development of drive products, drive systems, and high power supplies (5 kVA to 50 MVA). In 1996, he joined the Christian-Albrechts-University of Kiel, Kiel, Germany, as a Full Professor and the Head of the Institute for Power Electronics and Electrical Drives. Since 2013, he is pensioned, but still very active in research project and Ph.D. managing. Prof. Liserre is his successor as Head of the chair. His research and that of his team include power semiconductor applications, converters topologies, and variable-speed drives as well as their control. Topics are research in renewable energy conversion, particularly wind and solar energy, their grid integration, ac electric drives for automobiles, nonlinear control of drives, and diagnosis of drives and fault-tolerant drives. Many research projects are carried out with industrial partners. He is the author or coauthor of more than 220 papers and one book chapter.

Dr. Fuchs is an Associate Editor of the IEEE TRANSACTIONS ON POWER ELECTRONICS and Convenor and International Speaker for the Standardization of Power Electronics (Deutsche Kommission Elektrotechnik Elektronik Informationstechnik, International Electrotechnical Commission), as well as a member of Verband der Elektrotechnik Elektronik Informationstechnik and European Power Electronics and Drives Association.

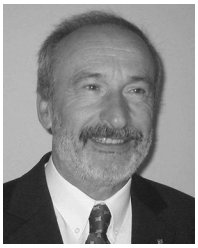

Marian P. Kazmierkowski (M'89–SM'91–F'98) received the M.S., Ph.D., and Dr. Sci. degrees in electrical engineering from the Institute of Control and Industrial Electronics (ICIE), Warsaw University of Technology, Warsaw, Poland, in 1968, 1972, and 1981, respectively.

From 1987 to 2008, he was the Director of ICIE. He has been the Head of the Centre of Excellence in Power Electronics and Intelligent Control for Energy Conservation at ICIE since 2003. In 1974, he made a three-month internship at Siemens in Vienna, and 1980–1984 he was at the RWTH Aachen as a Scholar of the Alexander von Humboldt Foundation. He is currently a Full Professor at ICIE and Consultant at the Electrotechnical Institute (IEl) in Warsaw.

Dr. Kazmierkowski was the Vice President of the IEEE Industrial Electronics Society (1999–2001) and the Editor-in-Chief of the IEEE TRANSACTIONS ON INDUSTRIAL ELECTRONICS (2004–2006). He received an Honorary Doctorate degree from the Aalborg University, Aalborg East, Denmark, in 2004, from the Institut National Polytechnique de Toulouse, Toulouse, France, in 2010, and from the University of Zielona Gora, Poland, in 2012. He received the Dr. Ing. Eugene Mittelmann Achievement Award from the IEEE Industrial Electronics Society in 2005 and the SIEMENS Research Award in Poland in 2007. In 2007, he was elected as the Corresponding Member of the Polish Academy of Sciences and later as the Dean of the Engineering Sciences Department, Polish Academy of Sciences (2010–2014).

Dierk Schroeder (M'84–SM'91–F'02) was born in Stendal, Germany, in 1941. He received the Dipl.-Ing. and Dr.-Ing. degrees from the Technical University of Darmstadt, Darmstadt, Germany, in 1966 and 1969, respectively.

He spent ten years in various positions at Asea Brown Boveri, Mannheim, Germany. In 1979, he was named the Professor and Chairman of the Institute of Electronics and Power Electronics at the University of Kaiserslautern. In 1983, he was named the Professor and Chairman of the Institute of Electrical Drive, Systems at the Technical University of Munich, Germany. During 2006–2009, he retired but still in the old position, and since 2009 he has been involved in writing books and giving lectures about Intelligent Strategies.